NUCL SCI TECH (2021) 32:141
https://doi.org/10.1007/s41365-021-00980-1

Performance evaluation of ultra-long lithium heat pipe using an improved lumped parameter model

Chong-Ju Hu[1,2,3] · Da-Li Yu[1] · Mei-Sheng He[1] · Hua-Ping Mei[1] · Jie Yu[1] · Tao-Sheng Li[1]

Received: 29 August 2021 / Revised: 26 October 2021 / Accepted: 28 October 2021 / Published online: 14 December 2021

Abstract Lithium heat pipes have broad applications in heat pipe cooling reactors and hypersonic vehicles owing to their ultra-high working temperature. In particular, when the length of the lithium heat pipe is ultra-long, the flow and heat transfer characteristics are more complex. In this study, an improved lumped parameter model that considers the Marangoni effect, bending effect, and different vapor flow patterns and Mach numbers was developed. Thereafter, the proposed model was verified using the University of New Mexico's Heat Pipe and HTPIPE models. Finally, the verified model was applied to simulate the steady-state operation of an ultra-long lithium heat pipe in a Heat Pipe-Segmented Thermoelectric Module Converters space reactor. Based on the results: (1) Vapor thermal resistance was dominant at low heating power and decreased with increasing heating power. The vapor flow inside the heat pipe developed from the laminar to the turbulent phase, whereas the liquid phase in the heat pipe was always laminar. (2) The vapor pressure drop caused by bending was approximately 22–23% of the total, and the bending effect on the liquid pressure drop could be ignored. (3) The Marangoni effect reduced the capillary limit by hindering the liquid reflux, especially at low vapor temperatures. Without considering the Marangoni effect, the capillary limit of the lithium heat pipe was overestimated by 9% when the vapor temperature was 1400 K. (4) The total thermal resistance of the heat pipe significantly increased with increasing adiabatic length when the vapor temperature was low. Further, the wick dryness increased with increasing adiabatic length at any vapor temperature. Such findings improve on current knowledge for the optimal design and safety analysis of a heat pipe reactor, which adopts ultra-long lithium heat pipes.

Keywords Lithium heat pipe · Bending effect · Marangoni effect · Capillary limit · Heat Pipe-Segmented Thermoelectric Module Converters (HP-STMC)

Nomenclature

A	Area [m^2]
a	Correction coefficient of velocity distribution
C	Thermal capacitance [(W s)/K]
c	Specific heat [J/(kg K)]
c_p	Specific heat at constant pressure [J/(mol K)]
c_v	Specific heat at constant volume [J/(mol K)]
f	Capillary correction coefficient
h_{fg}	Latent heat of vaporization/condensation [J/kg]
h	Convective heat transfer coefficient [W/(m^2·K)]
k	Thermal conductivity [W/(m·K)]
K	Permeability [m^2]
L	Length [m]
L^*	Flow inductance [m^{-1}]
$\dot{m}$	Mass flow rate [kg/s]
M	Working fluid mass [kg]
Ma	Mach number

This work was supported by the CASHIPS Director's Fund (No. YZJJ2021QN36) and the Key Research Program of the Chinese Academy of Sciences (No. ZDRW-KT-2019-1-0202).

✉ Da-Li Yu
dlyu@inest.cas.cn

[1] Institute of Nuclear Energy Safety Technology, Hefei Institutes of Physical Science, Chinese Academy of Sciences, Hefei 230031, China

[2] University of Science and Technology of China, Hefei 230026, China

[3] Suzhou University, Suzhou 234000, China

p	Pressure [Pa]
Q	Heating power [W]
r	Radius [m]
R	Resistance: thermal [K/W] or fluidic [Pa s/kg]
R^*	Ideal gas constant [J/(kg K)]
Re_r	Radial Reynolds number
Re_a	Axial Reynolds number
T	Temperature [K]
t	Time [s]
t^*	Annular wick thickness [m]
u	Velocity [m/s]
V	Volume [m^3]
ρ	Density [kg/m^3]
ε	Porosity
γ	Heat capacity ratio
ς	Local resistance coefficient
μ	Dynamic viscosity [Pa s]
η	Correction coefficient of flow regime
σ	Surface tension [Pa m]
δ	Annular gap [m]
θ	Wetting angle [°]

Subscripts

evap	Evaporator
cond	Condenser
pe	Evaporator pipe
pa	Adiabatic pipe
pc	Condenser pipe
we	Evaporator wick
wa	Adiabatic wick
wc	Condenser wick
ve	Evaporator vapor
va	Adiabatic vapor
vc	Condenser vapor
vd	Duct vapor
e	External
f	Cooling fluid
i	Internal
l	Liquid
w	Wick
m	Wire screen effective
eff	Effective
c	Capillary
v	Vapor
le	Evaporator liquid
lc	Condenser liquid
ld	Duct liquid
lwe	Evaporator liquid in wire screen
lwc	Condenser liquid in wire screen
adia	Adiabatic
vl	Vapor/liquid
leo	Maximum fluid mass in evaporator annular wick
leoo	Fluid mass in evaporator annular gap
pi	Inner radius of heat pipe wall
vl	Vapor/liquid

1 Introduction

Heat pipe reactor (HPR) is a promising energy supply technology for deep-space and deep-sea exploration missions [1–4]. HPR has the advantages of compact structure, high inherent safety, and modularization compared to conventional light water reactors. Bushman et al. from Massachusetts Institute of Technology (MIT) designed a 100 kWe Martian/Lunar surface reactor to operate for five effective full-power years (EFPY) to support extraterrestrial human exploration efforts [5]. Mcclure et al. from Los Alamos National Laboratory (LANL) designed a megawatt grade ground mobile heat pipe reactor to meet the power supply demand of 1–10 MW in war zones and remote areas [6]. Gu et al. from China Academy of Atomic Energy proposed a concept of heat pipe cooled modular fast reactor (HPCMR) for lunar surface to solve the energy supply problem of lunar base [7, 8].

High-temperature heat pipes comprising lithium, sodium, potassium, and other alkali metals as working fluids are often used in the design of HPR. Many experimental studies have investigated the operating performance of high-temperature heat pipes, which markedly influences the start-up, steady state, transient, and shutdown of the HPR.

Kemme tested the sonic limit of sodium, potassium, and cesium heat pipes and found that the temperature and working fluid type significantly impact the sonic limit [9]. Faghri fabricated, processed, and tested high-temperature sodium heat pipes with multiple heat sources and radiators and revealed that the start-up behavior of the liquid metal heat pipes is markedly dependent on the heat removal rate at the condenser [10]. Martin discovered that after 200 restart cycles, the performance of the start-up and operation processes of a sodium heat pipe remains unchanged [11]. Ling studied the performance of a rotating sodium heat pipe and found that the thermal conductivity is 60–100-fold higher than that of copper, and the temperature drop of a heat pipe with a small inner diameter is higher than that of a heat pipe with a large inner diameter [12]. Wang investigated the influences of heating power, inclination, filling rate, and heat transfer limits on the heat pipe performance of a potassium heat pipe and found that the heat transfer ability increases with increasing heating power. In addition, increasing the inclination angle will enhance heat transfer for low-filling-rate heat pipes, with the capillary limit and viscosity limit as the main factors affecting the heat transfer under uniform and constant heat flux [13–15].

As it is difficult to experimentally measure local parameters in the heat pipe, such as vapor velocity, vapor temperature, liquid velocity, and liquid pressure drop, many theoretical modes have been developed for high-temperature heat pipes.

Bowman studied transient and compressible air flow in a porous pipe and compared their model predictions with experimental data; the results showed good agreement. However, the transient time periods obtained in this study excluded the conjugate effects of the wall and wick. Therefore, the model cannot be used to simulate the transient performance of a heat pipe [16]. Cao proposed a transient and compressible vapor model coupled with a conduction model for the wall and wick of a heat pipe. However, the model neglects the effect of the liquid flow in the wick structure and cannot predict the capillary limit and flow parameters of the liquid working fluid, such as pressure and velocity [17]. Rice implemented a transient numerical analysis considering the flow in the wick and predicted the capillary limit [18].

For the simple and time-saving model, Zuo developed a "network" model for heat pipe transient performance; this model consists of several components that have different thermal resistances and dynamic responses [19]. Ferrandi proposed a lumped parameter model that considers liquid flow in the wick and can be used to predict the steady-state and transient performance of a heat pipe [20]. Kolliyil improved Ferrandi's model by considering the Marangoni effect. However, this model has drawbacks when employed to predict high-temperature heat pipes owing to the complex vapor flow characteristics and wick structure [21].

In summary, most of the existing high-temperature heat pipe numerical models do not consider the liquid flow in the wick. Therefore, this study developed an improved lumped parameter model for a high-temperature heat pipe that considers the influences of complex vapor flow, wick liquid flow, and Marangoni flow. Furthermore, the developed model was used to analyze the ultra-long lithium heat pipe in the HP-STMC space reactor. Finally, the flow and heat transfer performance, Marangoni effect, and heat pipe structure effect were discussed under different heating powers. This study mainly seeks to provide a method that can consider the complete heat transfer and fluid flow of high-temperature heat pipes, and be employed to study the internal operation mechanism of ultra-long lithium heat pipes.

2 Mathematical model

The model consists of solid and liquid regions. Each region is divided into a finite control volume, and each control volume is regarded as a node. The physical parameters of the control volume are equivalently loaded on the node, and the nodes are connected to each other by means of inductive, capacitive, and resistive elements for modeling different mechanisms. For example, the wall of the whole evaporation section has a control volume, which is characterized by a unique thermodynamic status. A set of first-order linear differential equations was established for each node, and all differential equations were solved simultaneously.

2.1 Solid region modeling

The solid region consists of a wall section and a wick section. Each part is composed of an evaporator, adiabatic section, and condenser. Therefore, the solid model is regarded as a six-node network system formed by six control volumes, and the nodes are connected by thermal resistance and heat capacity. The solid network system is shown in Fig. 1.

The axial and radial thermal resistances of the solid region are calculated using the following equations:

$$R_{\text{radial}} = \frac{\ln\left(r_{\text{e}}/r_{\text{i}}\right)}{2\pi kL}, \tag{1}$$

$$R_{\text{axial}} = \frac{L}{kA}, \tag{2}$$

where r_{e} and r_{i} represent the outer radius and inner radius of the control volume, respectively, A and L represent the cross-sectional area and the length of the control volume, respectively, and k represents the thermal conductivity of the control volume.

This study focuses on a lithium heat pipe for a space reactor, for which an annular wick is adopted in the analysis. The effective thermal conductivity and effective heat capacity of the wire screen mesh part of the wick were calculated using Eqs. (3–4). The effective thermal conductivity and effective heat capacity of the entire annulus wick were calculated using Eqs. (5–7) [22], and the heat capacities of other parts in the heat pipe were calculated using Eq. (8).

$$k_{\text{m}} = \frac{k_{\text{l}}[k_{\text{l}} + k_{\text{w}} - (1-\varepsilon_{\text{m}})(k_{\text{l}} - k_{\text{w}})]}{k_{\text{l}} + k_{\text{w}} + (1-\varepsilon_{\text{m}})(k_{\text{l}} - k_{\text{w}})}, \tag{3}$$

$$C_{\text{m}} = (\rho c)_{\text{m}} \cdot V_{\text{lw}} = [(1-\varepsilon_{\text{m}})(\rho c)_{\text{w}} + \varepsilon_{\text{m}}(\rho c)_{\text{l}}] \cdot V_{\text{lw}}, \tag{4}$$

$$k_{\text{eff}} = \frac{k_{\text{l}} k_{\text{m}}}{\varepsilon k_{\text{m}} + k_{\text{l}}(1-\varepsilon)}, \tag{5}$$

$$\varepsilon = \frac{V_{\text{l}} - V_{\text{lw}}}{V_{\text{l}}}, \tag{6}$$

$$C_{\text{eff}} = (\rho c)_{\text{eff}} V_{\text{l}} = [(1-\varepsilon)(\rho c)_{\text{m}} + \varepsilon(\rho c)_{\text{l}}]V_{\text{l}}, \tag{7}$$

$$C = \rho c V, \tag{8}$$

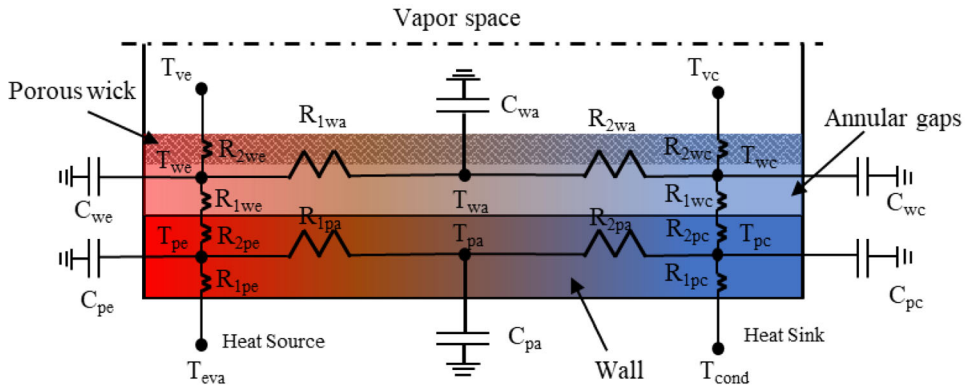

Fig. 1 (Color online) Network scheme for the solid model

where k_w and k_l represent the thermal conductivities of the wire screen mesh and working fluid, respectively; ρ_w and ρ_l represent the densities of the wire screen mesh and working fluid, respectively; c_w and c_l represent the specific heat of the wire screen mesh and working fluid, respectively; V_{lw} and V_l represent the volume of the wire screen mesh part of the wick and the whole annular wick, respectively; ρ, c, and V represent the density, specific heat, and volume of the control volume, respectively; and C is the thermal capacity of the control volume.

During the operation of the heat pipe, the properties of the working fluid in the wick's evaporator and condenser sections vary. Therefore, it is necessary to update C_m, ε, k_{eff}, C_{eff}, and V_{lw} after each time step.

The governing differential equation in the model for the six nodes in the solid region is depicted in Eq. (9).

$$C_i \frac{\mathrm{d}T_i}{\mathrm{d}t} = \pm \sum_{j=1, j\neq i}^{\text{neighbournodes}} \frac{|T_i - T_j|}{R_{ij}} \begin{cases} +\text{Heat incoming to node } i \\ -\text{Heat outgoing from node } i \end{cases} \tag{9}$$

2.2 Fluidic model

The physical mechanisms in the fluid region of the lithium heat pipe are complex. Therefore, it is necessary to simplify the governing equations. The assumptions adopted in this work are as follows:

(1) Liquid flow and vapor flow are one-dimensional.
(2) Liquid is incompressible and vapor is the ideal gas.
(3) The expansion and compression of the vapor are regarded as adiabatic processes.
(4) Liquid flow is considered laminar.
(5) Evaporation occurs in the evaporator and condensation occurs in the condenser only.
(6) The mass flow rate of the adiabatic section is constant.
(7) The temperature of the wire screen mesh is considered to be consistent with that of the adjacent liquid.

Figure 2a shows a schematic of the fluid model. The evaporator and condenser are regarded as the vapor storage tank and liquid storage tank, respectively. The mass transfer between the vapor storage tank and liquid storage tank was realized by evaporation or condensation. The vapor–vapor storage tank and the liquid–liquid storage tank are connected by the vapor and liquid ducts, respectively. Figure 2b shows a complete fluidic electrical scheme.

2.2.1 Vapor storage

According to assumption 2, vapor is considered as an ideal gas, described by equation $\frac{\partial p_v}{\partial \rho_v} = R^* T_v$. Equation (10) and Eq. (11) are the continuity equations for the evaporator and condenser, respectively:

$$\begin{aligned} \text{Evaporator: } & \frac{V_{ve}}{R^* T_{ve}} \frac{\mathrm{d}p_{ve}}{\mathrm{d}t} = \dot{m}_{evap} - \dot{m}_{vd} \\ & \rightarrow C_{ve} \frac{\mathrm{d}p_{ve}}{\mathrm{d}t} = \dot{m}_{evap} - \dot{m}_{vd}, \end{aligned} \tag{10}$$

$$\begin{aligned} \text{Condenser: } & \frac{V_{vc}}{R^* T_{vc}} \frac{\mathrm{d}p_{vc}}{\mathrm{d}t} = \dot{m}_{vd} - \dot{m}_{cond} \\ & \rightarrow C_{vc} \frac{\mathrm{d}p_{vc}}{\mathrm{d}t} = \dot{m}_{vd} - \dot{m}_{cond}, \end{aligned} \tag{11}$$

where V, C, p, T, R^* represent the tank volume, flow capacitance, pressure, temperature, and the vapor perfect gas constant, respectively, and $\dot{m}$ represents the mass flow rate.

According to the assumption of an adiabatic process $TP^{\frac{1-\gamma}{\gamma}} = \text{const}$, the relationship between the temperature and pressure in the vapor tank can be expressed using the following equations:

$$\frac{\mathrm{d}T_{ve}}{\mathrm{d}t} = \frac{\gamma - 1}{\gamma} \frac{T_{ve}}{p_{ve}} \frac{\mathrm{d}p_{ve}}{\mathrm{d}t}, \tag{12}$$

$$\frac{\mathrm{d}T_{vc}}{\mathrm{d}t} = \frac{\gamma - 1}{\gamma} \frac{T_{vc}}{p_{vc}} \frac{\mathrm{d}p_{vc}}{\mathrm{d}t}. \tag{13}$$

The adiabatic exponent γ is determined using:

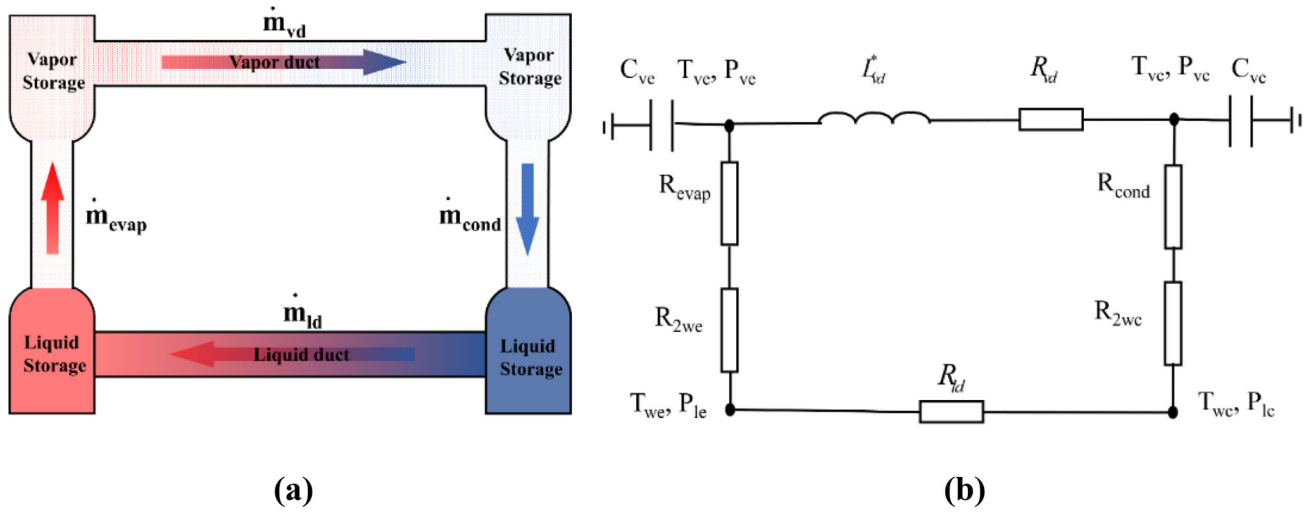

Fig. 2 (Color online) Lumped parameter fluid model: **a** Schematic. **b** Network diagram

$$\gamma(T_v) = \frac{c_p(T_v)}{c_v(T_v)}. \tag{14}$$

2.2.2 Vapor duct

As the vapor flow characteristics in the heat pipe are complex, the decreases in vapor pressure in the evaporator, adiabatic section, and condenser are calculated independently, and the effect of the local bending pressure drop is considered. According to the one-dimensional flow assumption, the momentum equation of the vapor flow in the vapor duct is:

$$\int_{L_{\text{eff}}} \frac{\partial p_{\text{vd}}}{\partial x} \mathrm{d}l = \int_{L_{\text{eff}}} \mu \frac{\partial^2 u_{\text{vd}}}{\partial x^2} \mathrm{d}l + \varsigma \frac{\rho_{\text{vd}} u_{\text{vd}}^2}{2} - \int_{L_{\text{eff}}} \rho \frac{\partial u_{\text{vd}}}{\partial t} \mathrm{d}l, \tag{15}$$

where L_{eff} represents the effective length and assumes

$$L_{\text{eff}} = (1/2 L_{\text{evap}}) + L_{\text{adia}} + (1/2 L_{\text{cond}}),$$

ς represents the local resistance coefficient, and u_{vd} represents the vapor flow rate.

The term on the left side of the equation can be rewritten as:

$$\int_{L_{\text{eff}}} \frac{\partial p_{\text{vd}}}{\partial x} \mathrm{d}l = p_{\text{ve}} - p_{\text{vc}}. \tag{16}$$

The viscous term is affected by vapor compressibility and flow pattern. Therefore, according to the theory of Chi [22], the pressure drops are calculated using the following equations:

$$-\int_{L_{\text{eff}}} \mu \frac{\partial^2 u_{\text{vd}}}{\partial x^2} \mathrm{d}l = R_{\text{vd}} \dot{m}_{\text{vd}},$$

$$R_{\text{vd}} = \begin{cases} 1 & Re_v \le 2300, Ma \le 0.2 \\ (1 + \frac{\gamma - 1}{2} Ma^2)^{-1/2} & Re_v \le 2300, Ma > 0.2 \\ 0.00238 (\frac{2 r_{\text{vd}} Q}{A_{\text{vd}} h_{\text{fg}} \mu_{\text{vd}}})^{3/4} & Re_v > 2300, Ma \le 0.2 \\ 0.00238 (\frac{2 r_{\text{vd}} Q}{A_{\text{vd}} h_{\text{fg}} \mu_{\text{vd}}})^{3/4} (1 + \frac{\gamma - 1}{2} Ma^2)^{-3/4} & Re_v > 2300, Ma > 0.2 \end{cases} \tag{17}$$

where Re_v represents the axial Reynolds number of vapor, Ma represents the Mach number of the vapor, A_{vd} represents the cross-sectional area of the vapor chamber, and h_{fg} represents the latent heat of vaporization of the working fluid.

Local pressure drop is written as:

$$\varsigma \frac{\rho_{\text{vd}} u_{\text{vd}}^2}{2} = \frac{\varsigma u_{\text{vd}}}{2 \pi r_{\text{vd}}^2} \dot{m}_{\text{vd}}. \tag{18}$$

Unsteady term is written as:

$$\int_{L_{\text{eff}}} \rho \frac{\partial u_{\text{vd}}}{\partial t} \mathrm{d}l = \rho_{\text{vd}} L_{\text{eff}} \frac{\mathrm{d}u_{\text{vd}}}{\mathrm{d}t} = \frac{L_{\text{eff}}}{\pi r_{\text{vd}}^2} \frac{\mathrm{d}\dot{m}_{\text{vd}}}{\mathrm{d}t} = L_{\text{vd}}^* \frac{\mathrm{d}\dot{m}_{\text{vd}}}{\mathrm{d}t}. \tag{19}$$

Thus, the momentum equation of the vapor flow in the vapor duct can be simplified as

$$L_{\text{vd}}^* \frac{\mathrm{d}\dot{m}_{\text{vd}}}{\mathrm{d}t} = p_{\text{ve}} - p_{\text{vc}} - R_{\text{vd}} \dot{m}_{\text{vd}}, \tag{20}$$

where R_{vd} and L_{vd}^* represent flow resistance and flow inductance, respectively.

2.2.3 Liquid duct

According to Darcy's law and considering the Marangoni effect, the momentum equation of the liquid flow in the liquid duct is described by:

$$\frac{\rho_{\mathrm{ld}}K}{\mu_{\mathrm{ld}}\varepsilon}\frac{\partial u_{\mathrm{ld}}}{\partial t}+u_{\mathrm{ld}}=-\frac{K}{\mu_{\mathrm{ld}}}\nabla p+\varepsilon\frac{t^{*}(T_{\mathrm{ve}}-T_{\mathrm{vc}})}{2\mu_{\mathrm{ld}}L_{\mathrm{eff}}}\nabla\sigma, \tag{21}$$

where K represents the annular wick permeability,ρ_{l} and μ_{l} represent the density and dynamic viscosity of the liquid, respectively; u_{l} represents the flow rate of the liquid; and T_{ve} and T_{vc} represent the evaporator and condenser temperatures, respectively.

For the annular wick, the fluid mainly flows back through the annular gap. As a result, only the annular gap flow is considered. Therefore, Eq. (21) can be simplified as follows:

$$\frac{\rho_{\mathrm{ld}}K}{\mu_{\mathrm{ld}}}\frac{\partial u_{\mathrm{ld}}}{\partial t}+u_{\mathrm{ld}}=-\frac{K}{\mu_{\mathrm{ld}}}\nabla p+\varepsilon\frac{t^{*}(T_{\mathrm{ve}}-T_{\mathrm{vc}})}{2\mu_{\mathrm{ld}}L_{\mathrm{eff}}}\nabla\sigma, \tag{22}$$

$$K=\frac{\delta^{2}}{12}, \tag{23}$$

where t^{*} represents the thickness of wick and δ represents the annular gap of wick.

The mass flow rate in the liquid duct can be determined using:

$$\dot{m}_{\mathrm{ld}}=\rho_{\mathrm{ld}}\pi[r_{\mathrm{pi}}^{2}-(r_{\mathrm{pi}}-\delta)^{2}]u_{\mathrm{ld}}, \tag{24}$$

where r_{pi} represents the inner radius of the heat pipe wall.

Combining Eqs. (22–24), the following momentum equation of the liquid flow in the liquid duct is obtained:

$$\begin{aligned}\frac{\mu_{\mathrm{ld}}L_{\mathrm{eff}}}{K\rho_{\mathrm{ld}}\pi[r_{\mathrm{pi}}^{2}-(r_{\mathrm{pi}}-\delta)^{2}]}\dot{m}_{\mathrm{ld}}&=p_{\mathrm{lc}}-p_{\mathrm{le}}\\&-\frac{\mu_{\mathrm{ld}}L_{\mathrm{eff}}}{K}\frac{\lambda_{\mathrm{m}}(T_{\mathrm{ev}}-T_{\mathrm{cv}})}{\rho_{\mathrm{ld}}\pi[r_{\mathrm{pi}}^{2}-(r_{\mathrm{pi}}-\delta)^{2}]},\end{aligned} \tag{25}$$

$$\lambda_{\mathrm{m}}=\frac{\rho_{\mathrm{ld}}A_{\mathrm{ld}}t^{*}}{2\mu_{\mathrm{ld}}L_{\mathrm{eff}}}\nabla\sigma_{\mathrm{liq/gas}}, \tag{26}$$

where A_{ld} represents the cross-sectional area of the annular wick.

Thus, Eq. (25) is simplified as:

$$R_{\mathrm{ld}}\dot{m}_{\mathrm{ld}}=p_{\mathrm{lc}}-p_{\mathrm{le}}-\frac{\mu_{\mathrm{ld}}L_{\mathrm{eff}}}{K}\frac{\lambda_{\mathrm{m}}(T_{\mathrm{ev}}-T_{\mathrm{cv}})}{\rho_{\mathrm{ld}}\pi[r_{\mathrm{pi}}^{2}-(r_{\mathrm{pi}}-\delta)^{2}]}, \tag{27}$$

where R_{ld} represents the liquid flow resistance.

2.2.4 Liquid storage

According to the continuity equation

$$\text{Evaporator: } \dot{m}_{\mathrm{ld}}-\dot{m}_{\mathrm{evap}}=\frac{\mathrm{d}M_{\mathrm{le}}}{\mathrm{d}t}, \tag{28}$$

$$\text{Condenser: } \dot{m}_{\mathrm{cond}}-\dot{m}_{\mathrm{ld}}=\frac{\mathrm{d}M_{\mathrm{lc}}}{\mathrm{d}t}. \tag{29}$$

M_{li} is given by

$$\text{Evaporator}: M_{\mathrm{le}}=\rho_{\mathrm{le}}(V_{\mathrm{lwe}}\varepsilon_{\mathrm{m}}+V_{\mathrm{le}}-V_{\mathrm{lwe}})L_{\mathrm{evap}}, \tag{30}$$

$$\text{Condenser}: M_{\mathrm{lc}}=\rho_{\mathrm{lc}}(V_{\mathrm{lwc}}\varepsilon_{\mathrm{m}}+V_{\mathrm{lc}}-V_{\mathrm{lwc}})L_{\mathrm{cond}}. \tag{31}$$

2.2.5 Liquid/vapor coupling

The capillary pressure difference on the interface obeys the Young–Laplace equation.

$$\Delta p_{\mathrm{vl}}=\frac{2\sigma\cos\theta}{r_{\mathrm{c}}} \tag{32}$$

where Δp_{vl} represents the two-phase pressure difference at the interface, σ represents the surface tension of the working fluid, θ represents the wetting angle, which is available in the literature [23], and r_{c} represents the capillary radius.

The relationship between the vapor pressure and the liquid pressure is given by:

$$\text{Evaporator: } p_{\mathrm{le}}=p_{\mathrm{ve}}-f\frac{2\sigma\cos\theta}{r_{\mathrm{c}}}, \tag{33}$$

$$\text{Condenser: } p_{\mathrm{lc}}=p_{\mathrm{vc}}, \tag{34}$$

where f represents the capillary correction coefficient [20], which considers the influence of the dryness level of the wick on the capillary pressure. f is obtained using the following equations:

$$\begin{cases}f=(1-\dfrac{M_{\mathrm{le}}-M_{\mathrm{leoo}}}{(M_{\mathrm{leo}}-M_{\mathrm{leoo}})_{\max}}) & \text{if } 0\le M_{\mathrm{le}}-M_{\mathrm{leoo}}\le(M_{\mathrm{le}}-M_{\mathrm{leoo}})_{\max}\\ f=\dfrac{p_{\mathrm{ve}}-p_{\mathrm{vc}}}{(2\sigma/r_{\mathrm{c}})} & \text{if } M_{\mathrm{le}}-M_{\mathrm{leoo}}\ge(M_{\mathrm{le}}-M_{\mathrm{leoo}})_{\max}\end{cases} \tag{35}$$

where M_{leoo} represents the working fluid mass in the annular gap of the evaporator, M_{leo} represents the maximum mass of the working fluid in the annular wick of the evaporator, and $(M_{\mathrm{leo}}-M_{\mathrm{leoo}})_{\max}$ represents the maximum working fluid mass in the wire screen mesh of the evaporator.

2.2.6 Solid/liquid coupling

Networks of the solid and fluid regions were coupled using mass flow rates of evaporation and condensation. According to assumption 7, the thermal resistance of evaporation and condensation is neglected, and the evaporation and condensation mass rates are given by

$$\dot{Q}_{\text{evap}} = \frac{T_{\text{we}} - T_{\text{ve}}}{R_{2\text{we}}} \rightarrow \dot{m}_{\text{evap}} = \frac{T_{\text{we}} - T_{\text{ve}}}{R_{2\text{we}} h_{\text{fg}}}, \tag{36}$$

$$\dot{Q}_{\text{cond}} = \frac{T_{\text{wc}} - T_{\text{vc}}}{R_{2\text{wc}}} \rightarrow \dot{m}_{\text{cond}} = \frac{T_{\text{wc}} - T_{\text{vc}}}{R_{2\text{wc}} h_{\text{fg}}}. \tag{37}$$

2.3 System of differential equations

Combining the above equations, a complete set of differential equations for the heat pipe is obtained:

$$\begin{gathered}
C_{\text{pe}} \frac{\mathrm{d}T_{\text{pe}}}{\mathrm{d}t} = Q - \frac{T_{\text{pe}} - T_{\text{pa}}}{R_{1\text{pa}}} - \frac{T_{\text{pe}} - T_{\text{we}}}{R_{2\text{pe}} + R_{1\text{we}}} \quad C_{\text{pa}} \frac{\mathrm{d}T_{\text{pa}}}{\mathrm{d}t} = \frac{T_{\text{pe}} - T_{\text{pa}}}{R_{1\text{pa}}} - \frac{T_{\text{pa}} - T_{\text{pc}}}{R_{2\text{pa}}} \\
C_{\text{pc}} \frac{\mathrm{d}T_{\text{pc}}}{\mathrm{d}t} = \frac{T_{\text{pa}} - T_{\text{pc}}}{R_{2\text{pa}}} + \frac{T_{\text{wc}} - T_{\text{pc}}}{R_{2\text{pc}} + R_{1\text{wc}}} - \frac{T_{\text{pc}} - T_{\text{f}}}{R_{1\text{pc}} + R_{\text{f}}} \quad C_{\text{we}} \frac{\mathrm{d}T_{\text{we}}}{\mathrm{d}t} = \frac{T_{\text{pe}} - T_{\text{we}}}{R_{2\text{pe}} + R_{1\text{we}}} - \frac{T_{\text{we}} - T_{\text{wa}}}{R_{1\text{wa}}} - \frac{T_{\text{we}} - T_{\text{ve}}}{R_{2\text{we}}} \\
C_{\text{wa}} \frac{\mathrm{d}T_{\text{wa}}}{\mathrm{d}t} = \frac{T_{\text{we}} - T_{\text{wa}}}{R_{1\text{wa}}} - \frac{T_{\text{wa}} - T_{\text{wc}}}{R_{2\text{wa}}} \quad C_{\text{wc}} \frac{\mathrm{d}T_{\text{wc}}}{\mathrm{d}t} = -\frac{T_{\text{wc}} - T_{\text{pc}}}{R_{2\text{pc}} + R_{1\text{wc}}} + \frac{T_{\text{wa}} - T_{\text{wc}}}{R_{2\text{wa}}} + \frac{T_{\text{vc}} - T_{\text{wc}}}{R_{2\text{wc}}} \\
R_{\text{ld}} \dot{m}_{\text{ld}} = p_{\text{lc}} - p_{\text{le}} - \frac{\mu_{\text{ld}} L_{\text{eff}}}{K} \frac{\lambda_{\text{m}} (T_{\text{ev}} - T_{\text{cv}})}{\rho_{\text{ld}} \pi (r_{\text{pi}}^2 - (r_{\text{pi}} - \delta)^2)} \quad \frac{\mathrm{d}M_{\text{le}}}{\mathrm{d}t} = \dot{m}_{\text{ld}} - \dot{m}_{\text{evap}} \\
\frac{\mathrm{d}M_{\text{lc}}}{\mathrm{d}t} = \dot{m}_{\text{cond}} - \dot{m}_{\text{ld}} \quad L_{\text{vd}}^{*} \frac{\mathrm{d}\dot{m}_{\text{vd}}}{\mathrm{d}t} = R_{\text{vd}} \dot{m}_{\text{vd}} + p_{\text{ve}} - p_{\text{vc}} \\
\frac{\mathrm{d}T_{\text{ve}}}{\mathrm{d}t} = \frac{\gamma - 1}{\gamma} \frac{T_{\text{ve}}}{p_{\text{ve}}} \frac{dp_{\text{ve}}}{dt} \quad \frac{\mathrm{d}T_{\text{vc}}}{\mathrm{d}t} = \frac{\gamma - 1}{\gamma} \frac{T_{\text{vc}}}{p_{\text{vc}}} \frac{\mathrm{d}p_{\text{vc}}}{\mathrm{d}t} \\
C_{\text{ve}} \frac{\mathrm{d}p_{\text{ve}}}{\mathrm{d}t} = \dot{m}_{\text{evap}} - \dot{m}_{\text{vd}} \quad C_{\text{vc}} \frac{\mathrm{d}p_{\text{vc}}}{\mathrm{d}t} = \dot{m}_{\text{vd}} - \dot{m}_{\text{cond}} \\
\dot{m}_{\text{evap}} = \frac{T_{\text{we}} - T_{\text{ve}}}{R_{2\text{we}} h_{\text{fg}}} \quad \dot{m}_{\text{cond}} = \frac{T_{\text{vc}} - T_{\text{wc}}}{R_{2\text{wc}} h_{\text{fg}}} \\
p_{\text{ve}} - p_{\text{le}} = f \frac{2\sigma \cos\theta}{r_{\text{c}}} \quad p_{\text{lc}} = p_{\text{vc}}
\end{gathered} \tag{38}$$

2.4 Numerical procedure

The differential equations with lumped parameters are expressed as follows:

$$\begin{cases} \dfrac{\mathrm{d}y}{\mathrm{d}t} = f(t, y) \\ y(t_0) = y_0 \end{cases} \tag{39}$$

where $y = (T_{\text{pe}}, T_{\text{pa}}, T_{\text{pc}}, T_{\text{we}}, T_{\text{wa}}, T_{\text{wc}}, \dot{m}_{\text{ld}}, \dot{m}_{\text{vd}}, M_{\text{le}}, M_{\text{lc}}, T_{\text{ve}}, T_{\text{vc}}, p_{\text{ve}}, p_{\text{vc}})$.

To solve the equations, the initial values of the parameters and boundary conditions should be determined. The boundary conditions used the input power in the evaporator and the equivalent thermal resistance in the condenser. The differential equations are discretized by the first-order difference method and solved using the Python program. The equations and boundary conditions are as follows:

$$y^{n+1} = y^n + \Delta t f(t^n, y^n), \tag{40}$$

Evaporator: $Q = Q_{\text{evap}}$, (41)

Condenser: $\begin{matrix} T_{\text{f}} = T_{\text{o}} \\ R_{\text{f}} = 1/(h_{\text{f}} A_{\text{f}}) \end{matrix}$, (42)

where Q_{evap} represents the heat input from the heat source to the evaporation section of the heat pipe, T_{o} represents the cooling medium temperature, h_{f} represents the convective heat transfer coefficient, and A_{f} represents the condenser heat dissipation area (m^2).

2.5 Model verification

To verify the accuracy of the improved lumped parameter model, the flow and heat transfer performance of the HP-STMC lithium heat pipe were simulated and compared with the existing UNM-HP and HTPIPE models in the literature [24]. The parameters of the lithium heat pipe are listed in Table 1. Figure 3a shows the variation in the vapor temperature and vapor temperature difference with different heating powers, and Fig. 3b shows the variation in the capillary limit with different vapor temperatures in the evaporator. The results obtained using the improved lumped parameter model align well with the results of the UNM-HP and HTPIPE models. The error between the calculated temperature difference of the

Table 1 Design parameters of the HP-STMCs power system reactor containing lithium heat pipes

Parameter	Value	Parameter	Value
Wall and porous wick	Mo-14%Re	Annular lithium gap (mm)	0.5
Heat pipe outer diameter (mm)	15	Wall thickness (mm)	0.4
Wick average porosity	0.69	Evaporator length (m)	0.45
Wick effective pore radius (μm)	12	Condenser length (m)	1.5
Porous wick thickness (mm)	0.2	Total length of heat pipe (m)	7.73
Vapor core radius (mm)	6.4	–	-

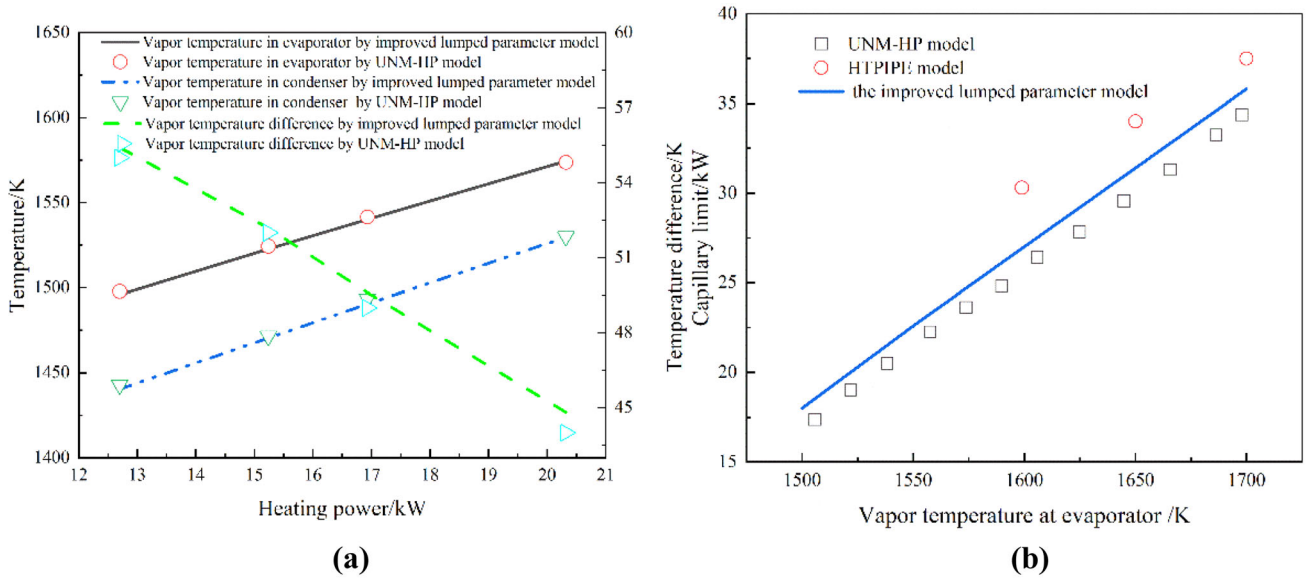

Fig. 3 (Color online) Comparisons between the lumped parameter model and existing models: **a** temperature and temperature difference. **b** Capillary limit

improved lumped parameters and that of the UMP-HP is no more than 1%, and the calculated capillary limit is approximately the average of the values from the UNM-HP and HTPIPE models.

3 Results and discussion

The performance of the ultra-long lithium heat pipe in the HP-STMC space reactor was evaluated using the improved lumped parameter model to primarily determine the influences of the bending structure, Marangoni flow, and the length of the adiabatic section on the heat pipe flow and heat transfer characteristics under different heating powers.

3.1 Flow and heat transfer performance analysis

Figure 4a shows the variations in the thermal resistance of the heat pipe with different heating powers. The results of the vapor thermal resistance and the total thermal resistance show the same trend, with both features varying sharply with increasing power. Such finding is consistent with the results reported in the literature [25]. The radial thermal resistance of the wall and wick increases slightly with increasing heating power as the thickness of the working fluid in the wick decreases. Therefore, the vapor thermal resistance is believed to mostly contribute to the total thermal resistance, for which further analysis is required.

The vapor thermal resistance decreased with an increase in the heating power. This is because when the heat sink is constant, the vapor temperature and density in the heat pipe increase with increasing heating power, which leads to a decrease in the vapor thermal resistance. When the vapor temperature was lower than 1600 K, the thermal resistance decreased rapidly with increasing temperature, while the temperature was higher than 1600 K, and the thermal

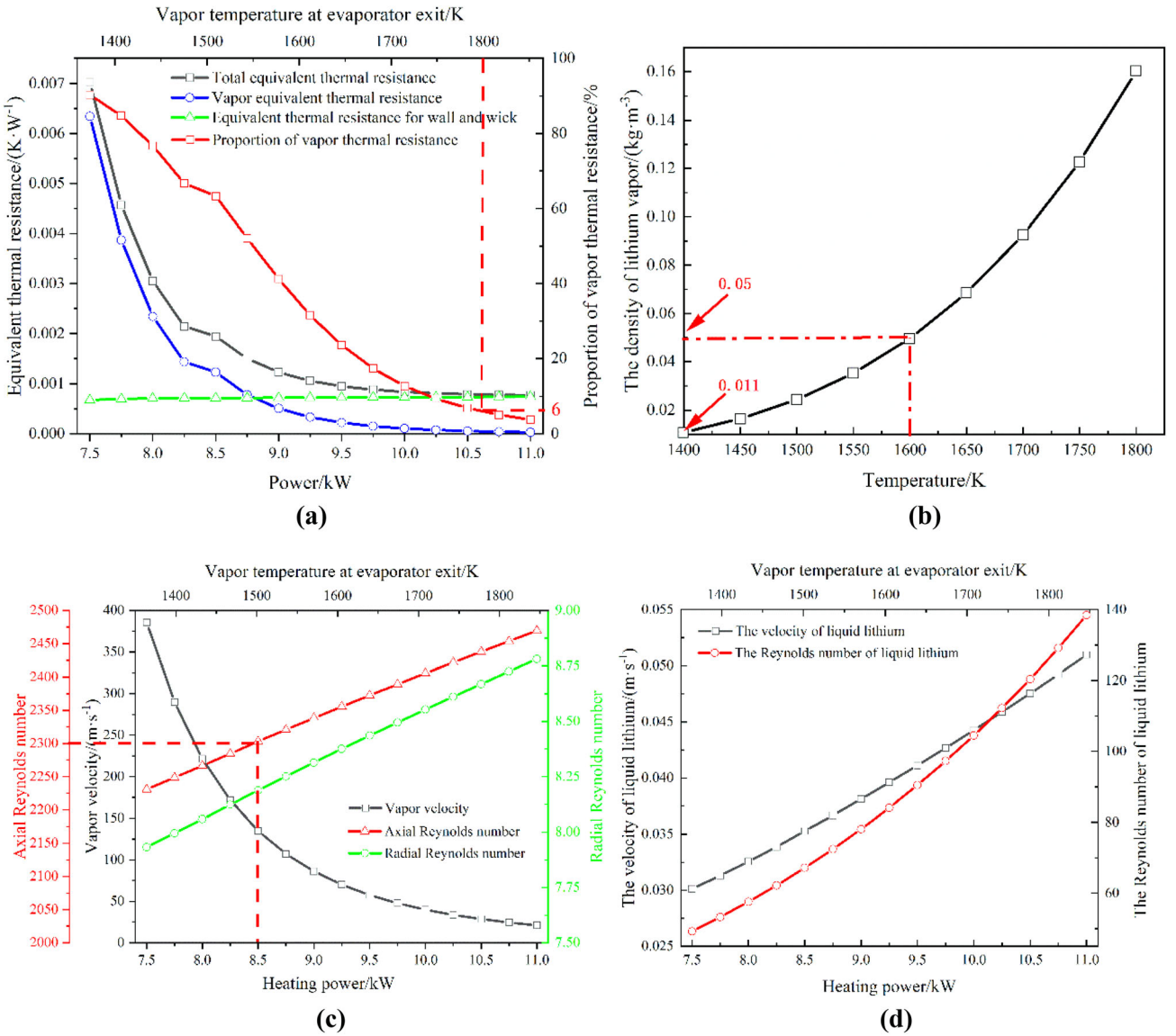

Fig. 4 (Color online) Flow and heat transfer parameters of heat pipe under different powers **a** Thermal resistance versus different powers under constant heat sink. **b** Lithium vapor density versus different temperatures. **c** Vapor velocity and Reynolds number versus different heating powers under constant heat sink. **d** Liquid velocity and Reynolds number versus different heating powers under constant heat sink

resistance was almost stable. Such occurrence is mainly due to the rapid growth of the lithium vapor density at low temperatures. As shown in Fig. 4b, the lithium vapor density increased nearly five times when the vapor temperature ranged from 1400 to 1600 K. Therefore, the lithium heat pipe may ideally function above 1600 K to obtain a good isothermal performance. The proportion of vapor thermal resistance decreased with increasing heating power. The proportion of vapor thermal resistance can reach nearly 90% of the total vapor pressure drop at a vapor temperature of 1400 K. Moreover, when the vapor temperature increases to 1800 K, the vapor thermal resistance still accounts for 6% of the total vapor pressure drop, which is due to the ultra-long insulation section and the local loss in the bending structure of the lithium heat pipe. Therefore, it is necessary to consider the vapor thermal resistance of an ultra-long lithium heat pipe.

Figure 4c shows the variations in the lithium vapor velocity and Reynolds number with different heating powers under a constant heat sink. The vapor flow rate decreased rapidly with increasing heating power. Although an increase in the heating power increases the mass flow rate of the circulating working fluid in the heat pipe, the density of lithium vapor increases rapidly with increasing temperature. As a result, the vapor flow rate does not increase and, instead, rapidly decreases. Based on the value

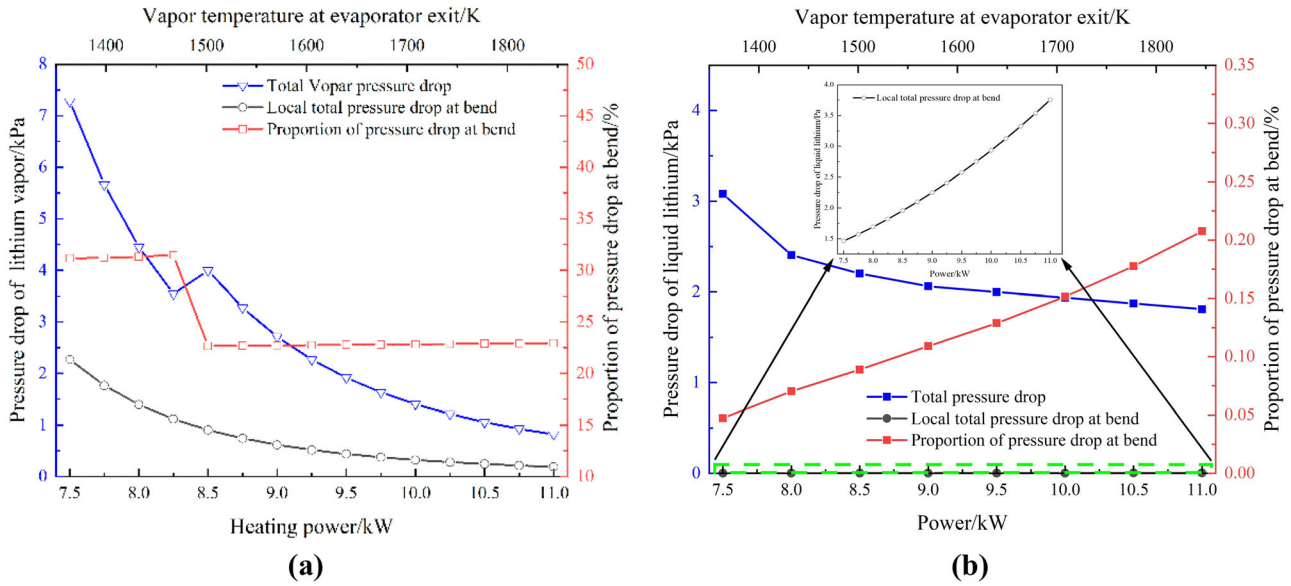

Fig. 5 (Color online) Pressure drop versus different heating powers under constant heat sink. **a** Vapor pressure drop. **b** Liquid pressure drop

of the vapor flow rate, the minimum flow rate was more than 20 m/s, and the maximum value was 370 m/s. Both the radial and axial Reynolds numbers increase with increasing heating power, and the vapor flow switches from laminar to turbulent with increasing axial Reynolds number. Hence, it is necessary to consider the turbulence effect in the vapor flow of lithium heat pipes.

Figure 4d shows the variations in the velocity and Reynolds number of the lithium liquid with different heating powers under a constant heat sink. The maximum velocity of liquid lithium is less than 0.05 m/s. Thus, the effect of convection on the heat conduction of liquid lithium can be ignored, which is consistent with the literature [26, 27]. The liquid Reynolds number increases with increasing heating power; however, the maximum value is less than 140. Therefore, in the modeling of a lithium heat pipe, the liquid phase can be considered as a laminar flow.

3.2 Bending analysis

Owing to bending, the heat pipe produces an additional local pressure drop. Figure 5a shows the variation in the vapor pressure drop with different heating powers under a constant heat sink. Under different heating powers, the working temperature of the heat pipe increased with increasing heating power, the flow rate of the vapor decreased continuously, and the total pressure drop and local pressure drop decreased. The proportion of local pressure drop increased slightly with increasing heating power. Of note, at a power of 8.5 kW, the proportion drops and the total pressure drop increases suddenly; this is because the vapor flow enters the turbulence region. The local pressure drop proportion accounts for approximately 20%–30% of the total vapor pressure drop; hence, bending has an obvious impact on the vapor pressure drop of the heat pipe.

Figure 5b shows the variation in the liquid pressure drop with different heating powers under constant heat sink. As the heating power increased, the total pressure drop decreased. When the heating power was lower than 9 kW, the total pressure drop changed significantly. This is mainly caused by the Marangoni effect, which will be analyzed later. The local pressure drop increased with increasing heating power. Owing to the extremely low liquid flow rate, the proportion of the local liquid pressure drop does not exceed 0.25% of the total liquid pressure drop. Therefore, the effect of bending on liquid flow can be ignored.

3.3 Influence of Marangoni flow

As surface tension depends on temperature, the non-uniform temperature distribution formed at the liquid–vapor interface could result in a surface tension gradient, which impacts the flow, and is referred to as the Marangoni effect. For liquid lithium, the surface tension decreased with increasing temperature. When the condenser temperature is lower than the temperature of the evaporator, the Marangoni effect causes the liquid in the evaporator to flow to the condenser, thereby preventing backflow of the liquid.

Figure 6a shows the variation in the liquid pressure drop and dryness of the wire screen mesh versus different heating powers under a constant heat sink. When the Marangoni effect is not considered, the pressure drop

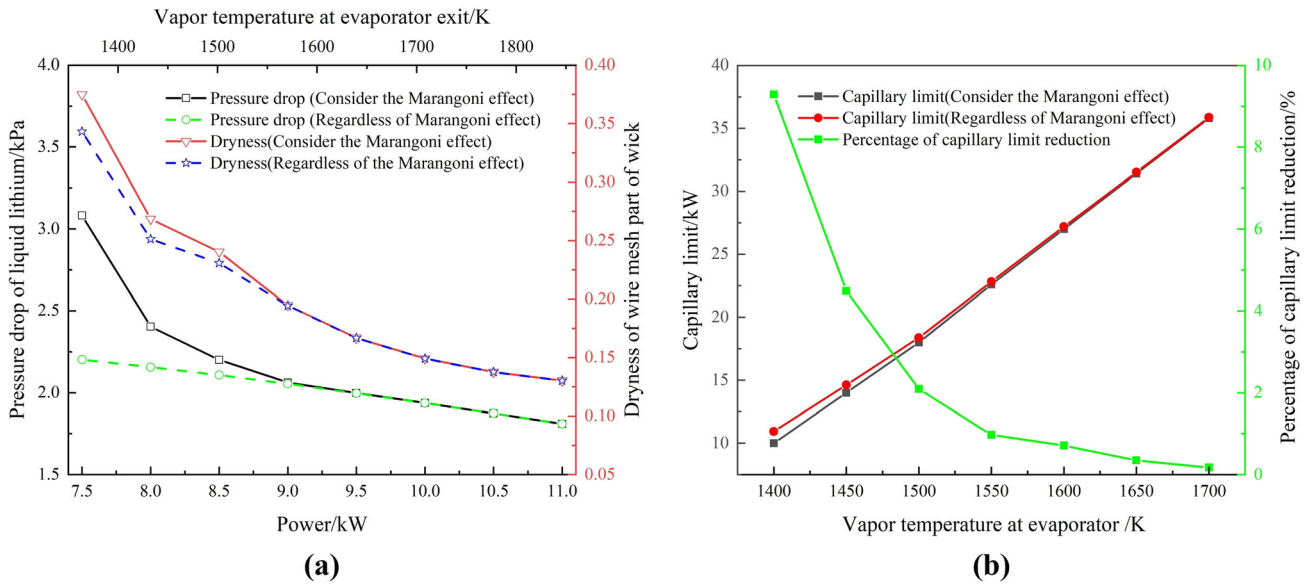

Fig. 6 (Color online) Effect of Marangoni flow on the performance of the heat pipe. **a** Liquid pressure drop and wire dryness versus different heating powers under constant heat sink **b** Capillary limit versus different vapor temperatures at the evaporator

decreases slightly with increasing heating power. Considering the Marangoni effect, when the heating power is lower than 9 kW, the pressure drop is markedly higher than that without considering Marangoni flow, and the maximum value can be nearly 40% larger than the former. This is mainly because a low heating power results in a low vapor temperature, and the axial temperature difference of vapor in the heat pipe is large; hence, the Marangoni effect is obvious. Because the pressure drop in the heat pipe is mainly based on the pressure difference of the vapor–liquid interface in the evaporator, a greater pressure drop of liquid and vapor lithium would cause a larger dryness of the wire mesh. Therefore, similar to the liquid pressure drop, the effect of the Marangoni effect on dryness is obvious at a lower power. When the heating power is 7.5 kW, the dryness considering the Marangoni effect is 10% more than that without considering the Marangoni effect.

Figure 6b shows the impact of the Marangoni effect on the capillary limit at different vapor temperatures in the evaporator. As the vapor flow resistance decreases with increasing temperature, the capillary limit increases with increasing working temperature, regardless of whether the Marangoni effect exists. For the same temperature, owing to the existence of the Marangoni effect, the liquid reflux resistance increases; hence, the capillary limit of the heat pipe considering the Marangoni effect is lower than that without considering the Marangoni effect, and the lower the temperature, the greater the difference. As shown in Fig. 6b, when the vapor temperature is 1400 K, the capillary limit considering the Marangoni effect is 9% lower than that without considering the Marangoni effect; however, when the vapor temperature increases to 1600 K, the Marangoni effect slightly affects the capillary limit.

3.4 Influence of adiabatic length

The thermal resistance of the heat pipe is generally composed of the radial thermal resistance of the wall and wick and the axial thermal resistance of the vapor. When the working temperature is low, the length of the adiabatic has a significant influence as the vapor axial thermal resistance contributes to the major portion. As shown in Fig. 7a, when the length of the adiabatic increases from 1 to 8 m for a vapor temperature of 1380 K, the thermal resistance increases by 110%. When the vapor temperature increased to 1930 K, the adiabatic length had little effect on the overall thermal resistance. Therefore, the adiabatic length should be reduced as much as possible when the working temperature is low.

Increasing the adiabatic length will increase the total pressure loss in the heat pipe; hence, the wick of the evaporator section needs to provide higher dryness to improve the pressure difference at the vapor–liquid interface of the evaporator. Figure 7b shows the effect of the adiabatic length on the wick dryness for different heating powers under a constant heat sink. When the adiabatic length increased from 1 to 8 m, the dryness increased by at least 300%. Therefore, the adiabatic length has a significant influence on the dryness over the entire working temperature range.

Figure 7c shows the proportion of the pressure drop at bending to the total pressure drop versus different adiabatic

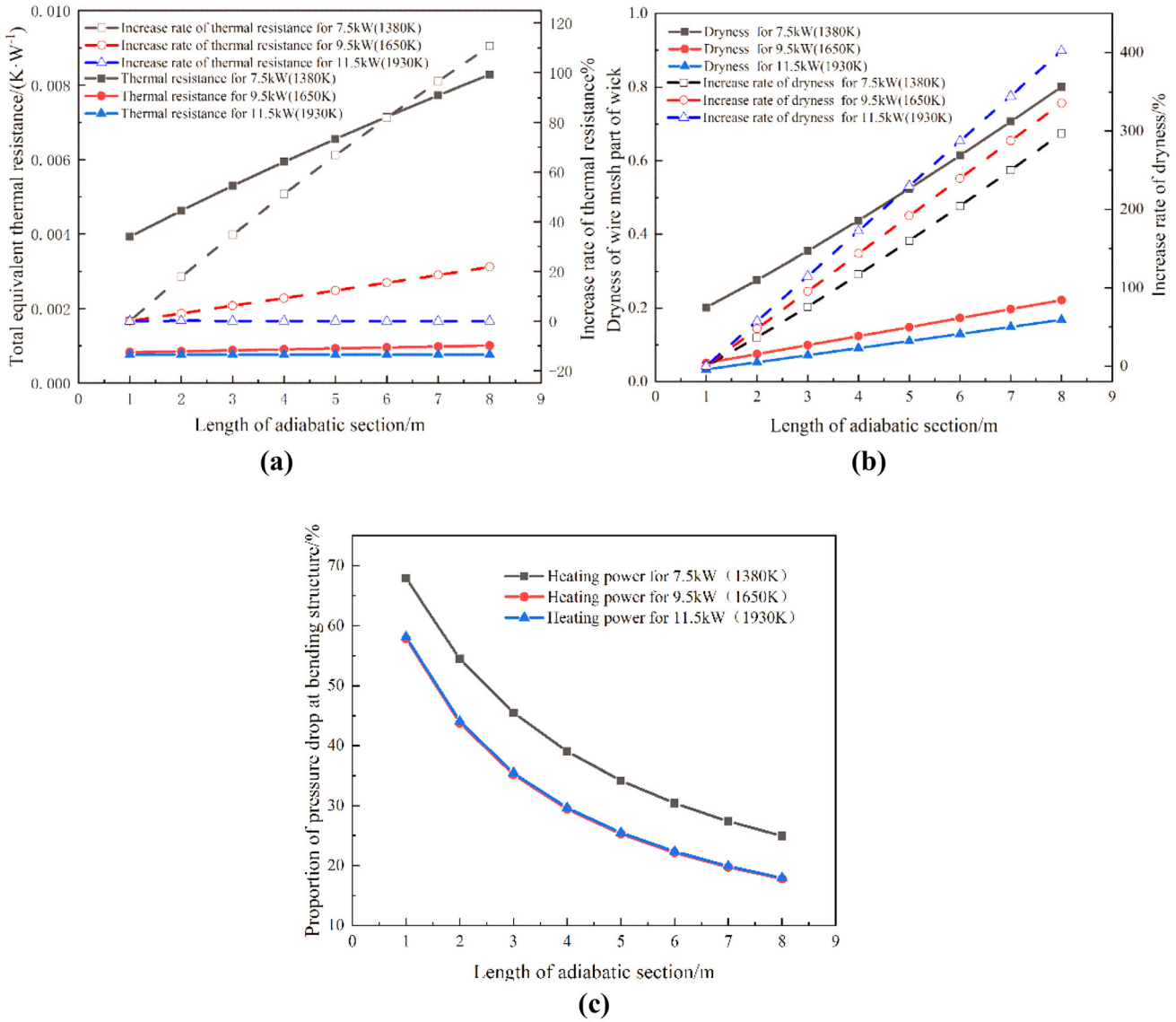

Fig. 7 Effect of adiabatic length on the performance of heat pipe: **a** Total equivalent thermal resistance versus different adiabatic lengths. **b** Wire dryness versus different adiabatic lengths. **c** Proportion of pressure drop at bend versus different adiabatic lengths

lengths under constant heat sink. For a certain adiabatic length, the proportion of pressure drop at bending decreased when the vapor temperature increased from 1380 to 1650 K, while the proportion remained almost constant when the vapor temperature increased from 1650 to 1930 K; this is mainly because the vapor flow rate is significantly affected by the vapor temperature at low temperatures. However, at high vapor temperatures, the vapor flow rate was unaffected by the vapor temperature. The proportion of the pressure drop at the bending of the total vapor pressure drop decreased with increasing adiabatic length. When the adiabatic length is 1 m, the maximum proportion can reach 70%.

4 Conclusion

Herein, an improved lumped parameter model was proposed, and the accuracy of the model was verified through a comparison with existing models. The model was then applied to the analysis of the ultra-long lithium heat pipe performance of the HP-STMCS space reactor. The influences of the Marangoni flow, bending effect, and adiabatic length on the performance of the heat pipe were studied. The main conclusions of this study are as follows:

(1) The total thermal resistance and vapor thermal resistance of the heat pipe decreased with increasing heating power and decreased nearly six times when the vapor temperature ranged from 1400 to 1600 K,

while the vapor thermal resistance remained almost constant for vapor temperatures higher than 1600 K. The radial thermal resistance increased slightly with increasing heating power, and the vapor thermal resistance reached 6% of the total vapor thermal resistance at 1800 K vapor temperature. Therefore, the vapor thermal resistance should not be neglected in the design and analysis of an ultra-long lithium heat pipe.

(2) The effect of liquid convection on the total heat transfer can be ignored because the liquid flow is generally laminar, and the vapor flow enters the turbulence from the laminar flow with increasing power.

(3) The vapor pressure drop caused by bending accounts for approximately 22%–23% of the total pressure drop, while the liquid pressure drop caused by bending accounts for less than 0.25%.

(4) The Marangoni effect can affect the liquid flow and the capillary limit of the heat pipe. Compared with the cases where the Marangoni effect was not considered, the capillary limit decreased by nearly 9% at a vapor temperature of 1400 K. However, when the vapor temperature increased to 1600 K, the calculated capillary limit considering the Marangoni effect decreased by less than 1%.

(5) The total thermal resistance of the heat pipe and wick dryness increased with increasing adiabatic length. When the heat pipe length increased from 1 to 8 m, the total thermal resistance increased by 110% at low vapor temperatures. However, this effect can be ignored at high vapor temperatures. The minimum increase in wick dryness was more than 300% for any vapor temperature. Bending has a significant influence on the heat pipe pressure drop when the adiabatic length is short and the vapor temperature is low. The maximum proportion of the pressure drop caused by bending was approximately 70%.

The above analysis results show that the improved lumped parameter method can effectively analyze the coupling characteristics of heat transfer and flow in a lithium heat pipe. To further study the distribution of thermodynamic parameters in the length direction of the lithium heat pipe, it is necessary to expand the quantity of the control volume, which will be the focus of our future work.

Author contribution All authors contributed to the study conception and design. Material preparation, data collection, and analysis were performed by Da-Li Yu, Chong-Ju Hu, Mei-Sheng He, and Hua-Ping Mei. The first draft of the manuscript was written by Chong-Ju Hu and all authors commented on previous versions of the manuscript. All authors read and approved the final manuscript.

References

1. Y. Yuan, J. Shan, B. Zhang et al., Study on startup characteristics of heat pipe cooled and AMTEC conversion space reactor system. Prog. Nucl. Energy **86**, 18–30 (2016). https://doi.org/10.1016/j.pnucene.2015.10.002
2. H. Sun, C.L. Wang, P. Ma et al., Conceptual design and analysis of a multipurpose micro nuclear reactor power source. Ann. Nucl. Energy **121**, 118–127 (2018). https://doi.org/10.1016/j.anucene.2018.07.025
3. P.R. Mcclure, D.D. Dixon, D.I. Poston et al., U.S. Patent 14/773, 405, 15 Apr 2014. https://www.freepatentsonline.com/W02014176069.pdf
4. A. Faghri, *Heat pipe science and technology* (CRC Press, Washington DC, 1995), pp. 41–55
5. A. Bushman, D. M. Carpenter, T. S. Ellis et al., The martian surface reactor: an advanced nuclear power station for manned extraterrestrial exploration. Technical Report MIT-NSA-TR-003, (2004). https://hdl.handle.net/1721.1/67634
6. P. R. Mcclure, V.R. Dasari, R.S. Reid et al., Design of megawatt power level heat pipe reactors. Technical Report LA-UR-15–28840 (2015). https://doi.org/10.2172/1226133
7. H. Gu, S. Z. Zhao, Z.Y. Sun et al., A heat pipe cooled modular reactor concept for Manned Lunar Base Application, In Proceedings of ICONE21 (Chengdu, China, 29 July - 2 August, 2013). https://doi.org/10.1115/ICONE21-16006
8. H. Gu, G. Jian, C.Z. Yao, *Space safety is no accident* (Springer International Publishing, Switzerland, 2015)
9. J.E. Kemme, Ultimate heat-pipe performance. IEEE Trans. Electron Devices **16**, 717–723 (1969). https://doi.org/10.1109/T-ED.1969.16845
10. Y. Cao, A. Faghri, Simulation of the early startup period of high-temperature heat pipes from the frozen state by a rarefied vapor self-diffusion model. J. Heat Transf.-Trans. ASME **115**, 239–245 (1993). https://doi.org/10.1115/1.2910655
11. J. Martin, O. Mireles, R. Reid, Multiple restart testing of a stainless steel sodium heat pipe module. AIP Conf. Proc. **746**, 150 (2005). https://doi.org/10.1063/1.1867129
12. J. Ling, Y.D. Cao, A.P. Lopez, Experimental investigations of radially rotating miniature high-temperature heat pipes. J. Heat Transf.- Trans. ASME **12**, 113–119 (2001)
13. C.L. Wang, L.R. Zhang, X. Liu et al., Experimental study on startup performance of high temperature potassium heat pipe at different inclination angles and input powers for nuclear reactor application. Ann. Nucl. Energy **136**, 107051 (2020). https://doi.org/10.1016/j.anucene.2019.107051
14. Z.X. Tian, X. Liu, C.L. Wang et al., Experimental investigation on the heat transfer performance of high-temperature potassium heat pipe for nuclear reactor. Nucl. Eng. Des. **378**, 111182 (2021). https://doi.org/10.1016/j.nucengdes.2021.111182
15. C.L. Wang, X. Liu, M.H. Liu et al., Experimental study on heat transfer limit of high temperature potassium heat pipe for advanced reactors. Ann. Nucl. Energy **151**, 107935 (2021). https://doi.org/10.1016/j.anucene.2020.107935
16. W. J. Bowman, Simulated heat pipe vapor dynamics (Air Force Institute of Technology, Dayton, 1987)
17. Y. Cao, A. Faghri, Transient multidimensional analysis of non-conventional heat pipes with uniform and nonuniform heat distributions. J. Heat Transf.-Trans ASME **113**, 995–1002 (1991). https://doi.org/10.1115/1.2911233

18. J. Rice, A. Faghri, Analysis of screen wick heat pipes, including capillary dry-out limitations. J. Thermophys. Heat Transf. **21**, 475–486 (2007). https://doi.org/10.2514/1.24809
19. Z.J. Zuo, A. Faghri, A network thermodynamic analysis of the heat pipe. Int. J. Heat Mass Transf. **41**, 1473–1484 (1998). https://doi.org/10.1016/S0017-9310(97)00220-2
20. C. Ferrandi, F. Iorizzo, M. Mameli et al., Lumped parameter model of sintered heat pipe: transient numerical analysis and validation. Appl. Therm. Eng. **50**, 1280–1290 (2013). https://doi.org/10.1016/j.applthermaleng.2012.07.022
21. J.J. Kolliyil, N. Yarramsetty, C. Balaji, Numerical modeling of a wicked heat pipe using lumped parameter network incorporating the marangoni effect. Heat Transf. Eng. **42**, 1–15 (2020). https://doi.org/10.1080/01457632.2020.1735799
22. S.W. Chi, *Heat pipe theory and practice* (Hemisphere Publishing Corp, New York, 1976), pp. 186–214
23. H.Q. Li, X.B. Jiang, L.X. Chen et al., Heat transfer capability analysis of heat pipe for space reactor. Atmoic Energy Sci. Technol. **49**, 89–95 (2015). https://doi.org/10.7538/yzk.2015.49.01.0089 (**in Chinese**)
24. J.M. Tournier, M.S. El-Genk, Reactor lithium heat pipes for HP-STMCs space reactor power system. AIP Conf. Proc. **699**, 781–792 (2004). https://doi.org/10.1063/1.1649643
25. Z.X. Tian, X. Liu, C.L. Wang et al., Study on heat transfer performance of high temperature potassium heat pipe at steady state. Atmoic Energy Sci. Technol. **54**, 1771–1778 (2020). https://doi.org/10.7538/yzk.2019.youxian.0767 (**in Chinese**)
26. M.M. Chen, A. Faghri, An analysis of the vapor flow and the heat conduction through the liquid-wick and pipe wall in a heat pipe with single or multiple heat sources. Int. J. Heat Mass Transf **33**, 1945–1955 (1990). https://doi.org/10.1016/0017-9310(90)90226-K
27. Z.Q. Zhang, X.M. Chai, C.L. Wang et al., Numerical investigation on startup characteristics of high temperature heat pipe for nuclear reactor. Nucl. Eng. Des. **378**, 111180 (2021). https://doi.org/10.1016/j.nucengdes.2021.111180